nature portfolio

https://doi.org/10.1038/s41928-022-00747-5

Supplementary information

Broadband convolutional processing using band-alignment-tunable heterostructures

In the format provided by the authors and unedited

Supplementary Information

Broadband convolutional processing using band-alignment-tunable heterostructures

Lejing Pi[1,#], Pengfei Wang[2,#], Shi-Jun Liang[2,#], Peng Luo[1], Haoyun Wang[1], Dongyan Li[1], Zexin Li[1], Ping Chen[1], Xing Zhou[1✉], Feng Miao[2✉] and Tianyou Zhai[1✉]

[1]State Key Laboratory of Material Processing and Die & Mould Technology, School of Materials Science and Engineering, Huazhong University of Science and Technology, Wuhan 430074, P. R. China

[2]Institute of Brain-inspired Intelligence, National Laboratory of Solid State Microstructures, School of Physics, Collaborative Innovation Center of Advanced Microstructures, Nanjing University, Nanjing 210093, P. R. China

[#]These authors equally contributed to this work: L.J.P., P.F.W., S.-J.L.

[✉]Correspondence Email: zhoux0903@hust.edu.cn (X.Z.); miao@nju.edu.cn (F.M.); zhaity@hust.edu.cn (T.Y.Z.)

Table of contents

Supplementary Fig. 1 | Characterization of the $PdSe_2$/$MoTe_2$ heterostructure

Supplementary Fig. 2 | Cross-sectional transmission electron microscopy images of the $PdSe_2$/$MoTe_2$ heterostructure

Supplementary Fig. 3 | Electrical characteristics of the $PdSe_2$/$MoTe_2$ heterostructure.

Supplementary Fig. 4 | Stable positive and negative photovoltaic effects at different wavelengths (365 nm, 532 nm and 980 nm)

Supplementary Fig. 5 | The reproducibility test of positive and negative photovoltaic photoresponse from three new devices

Supplementary Fig. 6 | Ultra-fast response characterization at 532 nm and 365 nm

Supplementary Fig. 7 | The optical image and scanning photocurrent mapping of the heterostructure device

Supplementary Fig. 8 | The false-color plot of gate-dependent photocurrent under dark and different wavelengths (365 nm, 532 nm and 980 nm) at variational V_{ds}

Supplementary Fig. 9 | Illustration of the Vis and UV characteristics of $PdSe_2$/$MoTe_2$ heterostructures for in-sensor broadband convolution processing

Supplementary Fig. 10 | Simulated results of two-dimensional broadband convolution operations for Jasper Ridge datasets

Supplementary Fig. 11 | Two-dimensional broadband convolution operations for the KSC and urban scenes

Supplementary Fig. 12 | Partially broadband and corresponding single-band image dataset for classifier training

Supplementary Fig. 13 | Schematic diagram of the training process for broadband and single-band image sensors

Supplementary Fig. 14 | Flow chart for the training algorithm

Supplementary Fig. 15 | The weights distribution of the kernels varies with the number of training epoch

Supplementary Fig. 16 | Comparison of the total output photocurrent under training epoch 1 and epoch 10

Supplementary Fig. 17 | The average output photocurrent for different input letters varies with number of training epoch

Supplementary Fig. 18 | The circuit scheme based on 2D heterostructure devices array for implementing convolution processing

Supplementary Table 1 | The total output photocurrent obtained for different images during the training process for convolution kernel ‘h’

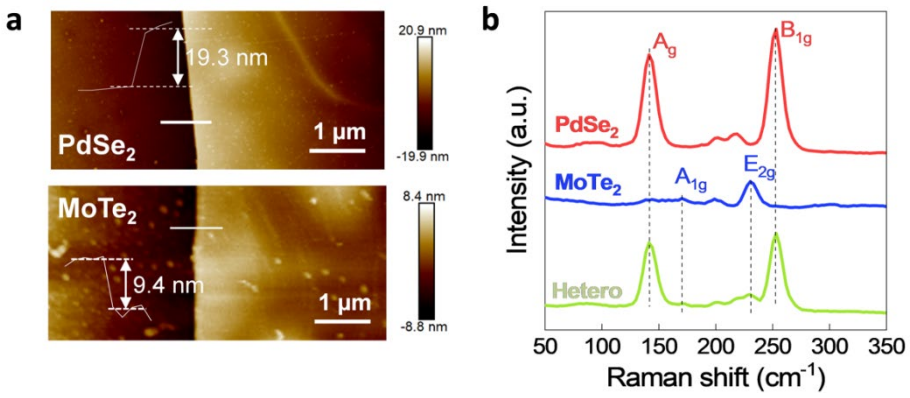

Supplementary Fig. 1. Characterization of the $PdSe_2$/$MoTe_2$ heterostructure. a, Atomic force microscopy images of the $PdSe_2$/$MoTe_2$ heterostructure, where the thickness of the $PdSe_2$ and $MoTe_2$ flakes is approximately 19.3 nm (32 layers) and 9.4 nm (13 layers), respectively. **b,** Raman spectra for the $PdSe_2$/$MoTe_2$ heterostructure, individual $PdSe_2$ and $MoTe_2$.

The Raman spectra collected in the isolated $PdSe_2$, $MoTe_2$ and overlapping junction regions are consistent with previous work[1,2]. Two main Raman peaks can be observed at 142 cm^{-1} and 256 cm^{-1}, corresponding to A_g and B_{1g} patterns of $PdSe_2$, respectively, whereas the Raman spectrum for the $MoTe_2$ flakes exhibits A_{1g} (168 cm^{-1}) and E_{2g}^1 (236 cm^{-1}) peaks. There is no obvious displacement of the characteristic peaks for the overlapping heterostructure region, indicating the high quality of the heterostructure after mechanical exfoliation and controllable dry transfer.

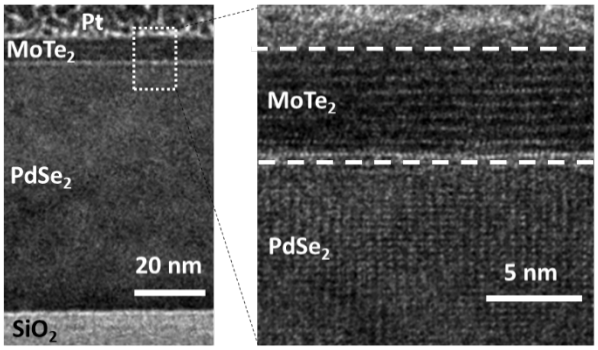

Supplementary Fig. 2. Cross-sectional transmission electron microscopy image of the $PdSe_2/MoTe_2$ heterostructure, where the interface is atomically sharp.

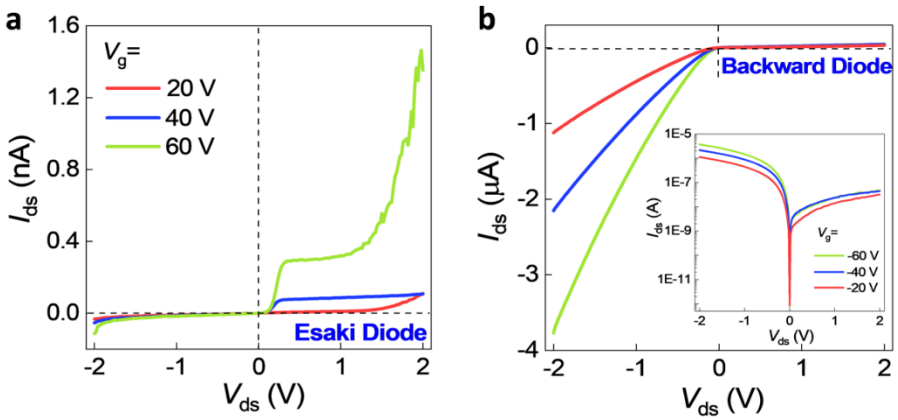

Supplementary Fig. 3. Electrical characteristics of the $PdSe_2/MoTe_2$ heterostructure. a, I_{ds}–V_{ds} curves for the device at V_g = 20 V, 40 V, and 60 V, which show the Esaki diode behaviour. **b,** Backward-diode behaviour for the I_{ds}–V_{ds} characteristics at V_g = -20 V, -40 V, and -60 V.

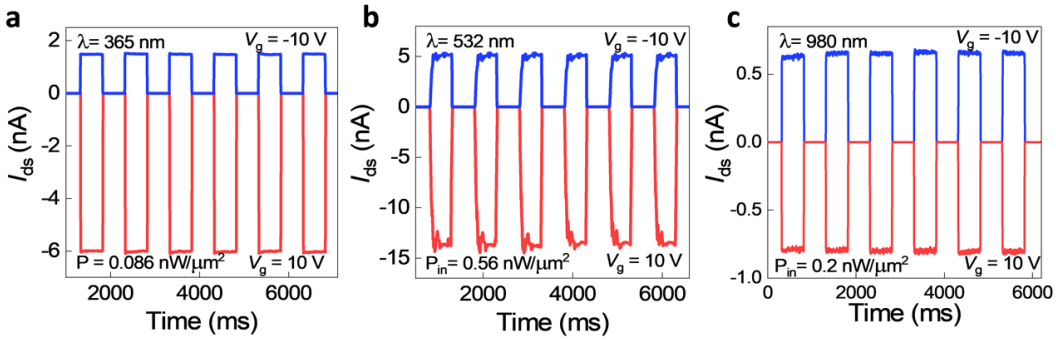

Supplementary Fig. 4. Stable positive and negative photovoltaic effects at different wavelengths (365 nm, 532 nm, and 980 nm). Time-resolved photovoltaic response of the heterostructure at V_g = -10 V and V_g = 10 V under illumination at a wavelength of 365 nm **(a)**, 532 nm **(b)** and 980 nm **(c)** respectively.

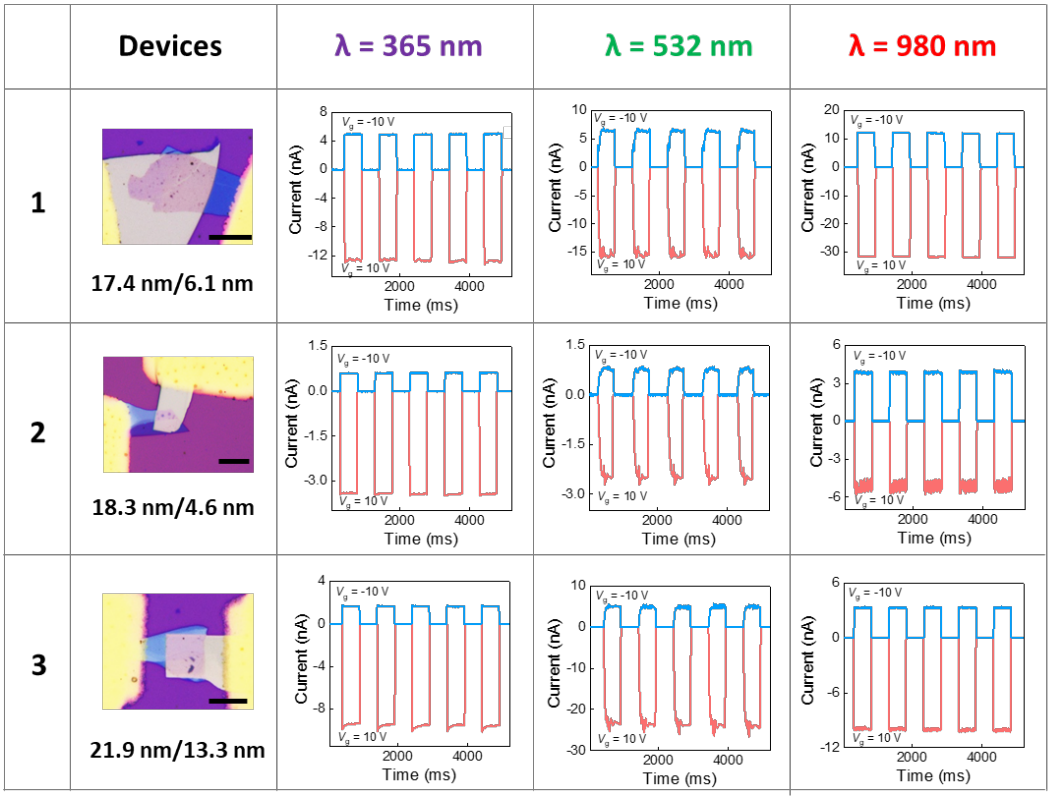

Supplementary Fig. 5. The reproducibility test of positive and negative photovoltaic photoresponse from three new devices under different wavelengths at V_g = -10 V and V_g = 10 V. The light intensity is 0.19 nW/μm^2 (365 nm), 0.45 nW/μm^2 (532 nm) and 4.6 nW/μm^2 (980 nm), respectively. The thickness of materials is labelled beneath the optical images of $PdSe_2/MoTe_2$ heterostructure device, and the scale bar is 10 μm.

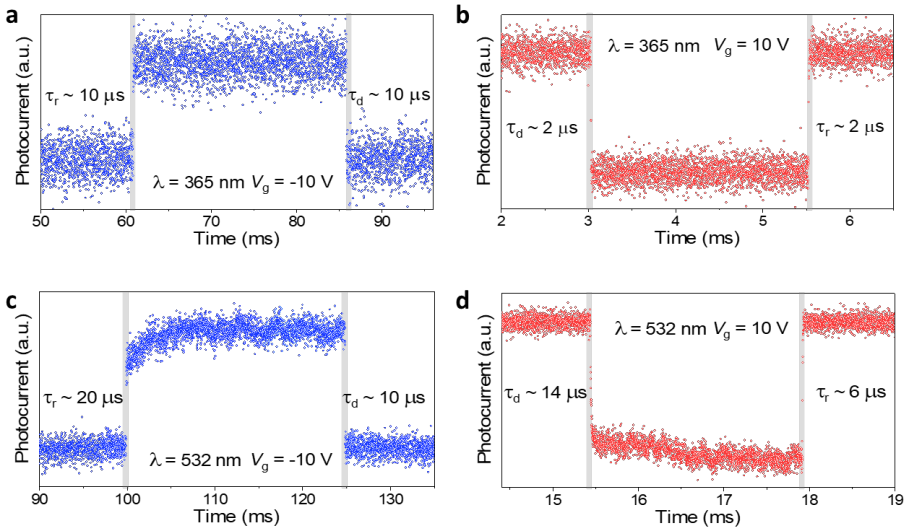

Supplementary Fig. 6. Ultra-fast response characterization at 532 nm and 365 nm. Rise (**a**) and decay time (**b**) for the positive and negative photovoltaic effects using an ultrafast mode for 365 nm, respectively. Rise (**c**) and decay time (**d**) using an ultrafast mode for 532 nm. The response speed, usually represented by rise time (or decay time), is defined as the time required for the net photocurrent to increase from 10% to 90% (or decrease from 90% to 10%).

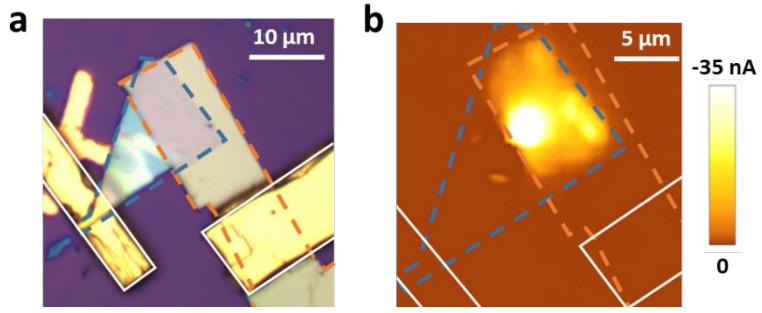

Supplementary Fig. 7. The optical image (a) and scanning photocurrent mapping (b) of the heterostructure device under laser illumination with the laser spot size of ~1 μm at V_{ds} = 0 V, where only the overlapped area of the heterostructure shows sensitivity to light, and almost no photocurrent has been observed in the contact area of electrodes. This indicates that the photocurrent is generated at the heterojunction through photovoltaic effect.

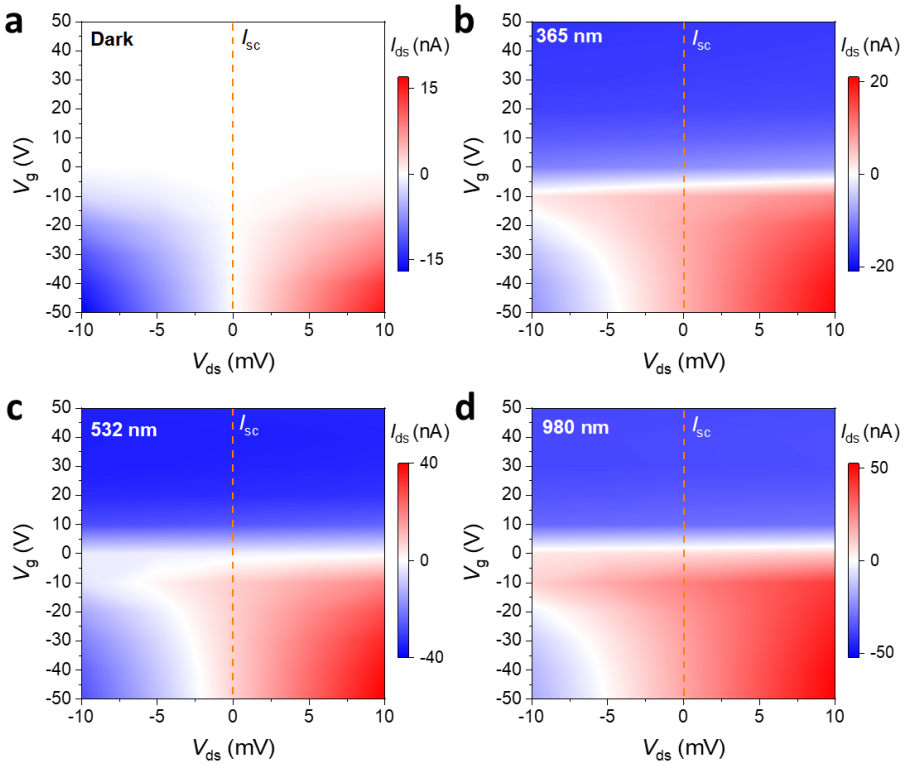

Supplementary Fig. 8. The false-color plot of gate-dependent photocurrent under dark (a) and different wavelengths at variational V_{ds}, including 365 nm (b), 532 nm (c) and 980 nm (d). The photovoltaic current remains stable under different wavelengths via modulating V_g dramatically (-50 V ~ 50 V), which means that the gate-tunable photocurrent does not originate from the asymmetric Schottky contacts.

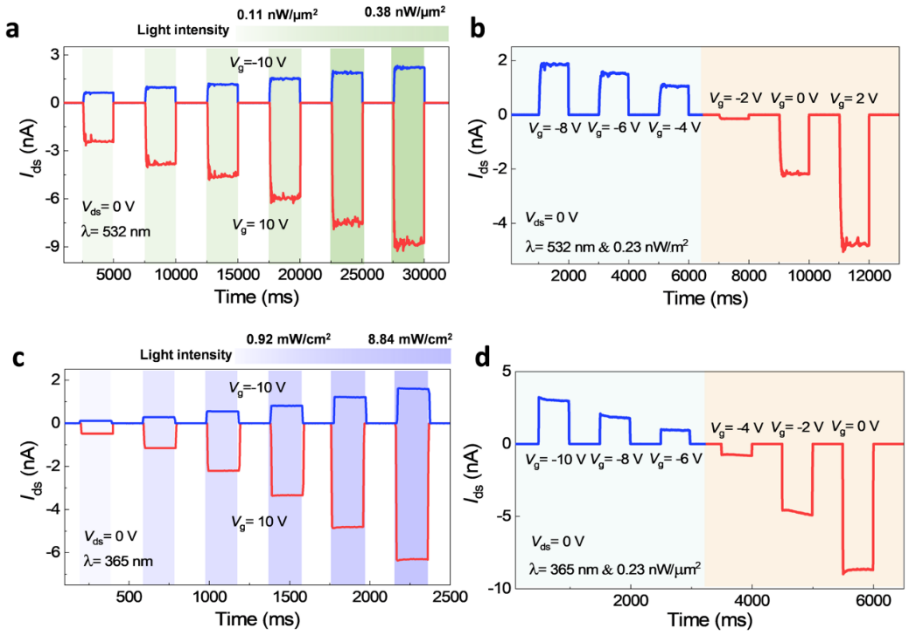

Supplementary Fig. 9. Illustration of the Vis and UV characteristics of $PdSe_2/MoTe_2$ heterostructures for in-sensor broadband convolution processing. Positive and negative photoresponses under different light intensities at a wavelength of 532 nm (**a**) and 365 nm (**c**) (indicated by shadow areas) at V_g = -10 V and 10 V, respectively. Positive and negative photoresponse conversion at different gate voltages under illumination at 532 nm (**b**) and 365 nm (**d**) with a power density of 0.23 nW/μm^2.

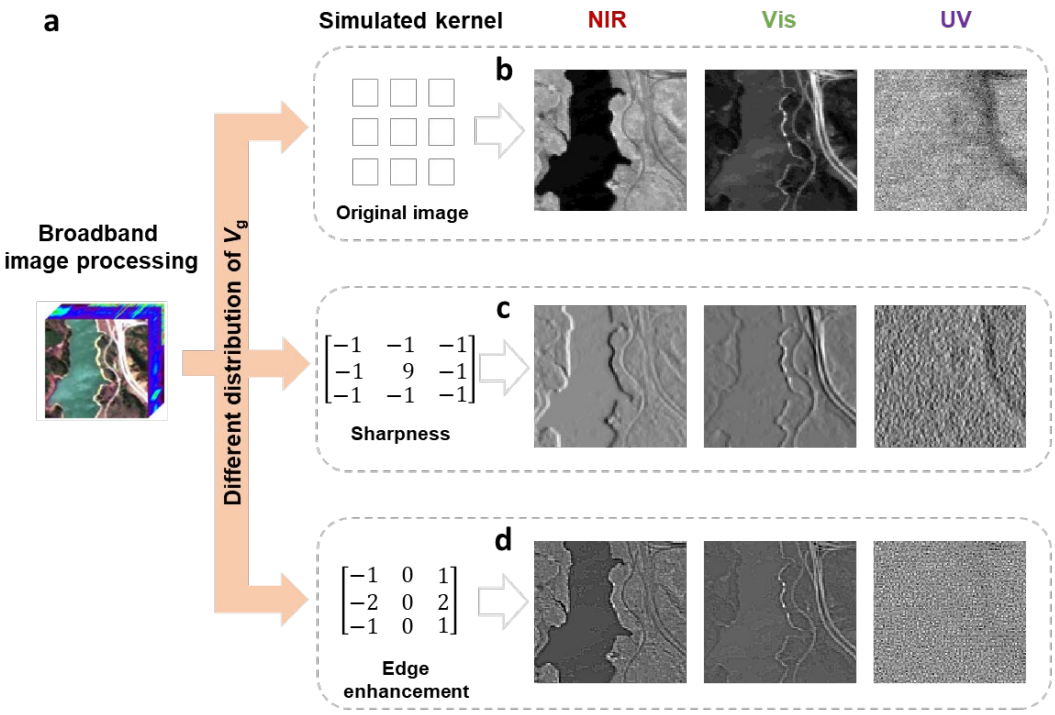

Supplementary Fig. 10. Simulated results of two-dimensional broadband convolution operations for Jasper Ridge datasets. a, Demonstration of different image processing operations (*i.e.*, edge enhancement and sharpness) with three different wavelengths (UV, Vis, NIR) by simulated kernels. **b,** Original image. **c,** Sharpness. **d,** Edge enhancement. Photo credits: https://rslab.ut.ac.ir/data.

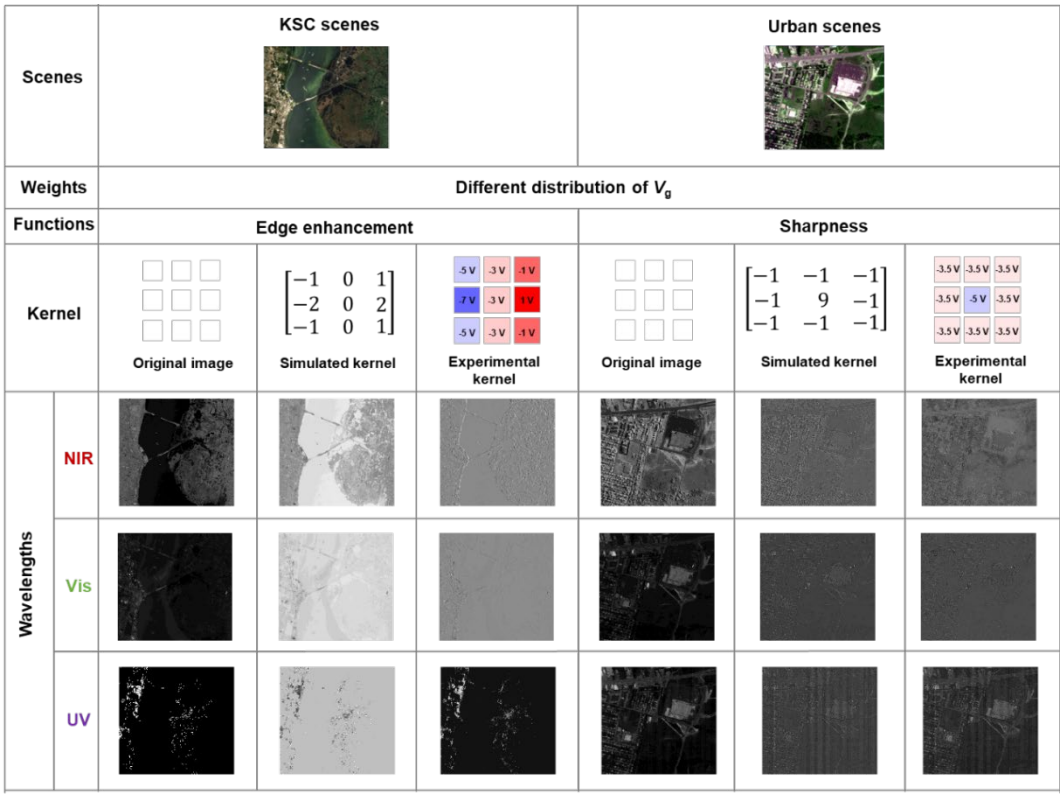

Supplementary Fig. 11. Two-dimensional broadband convolution operations for the KSC and urban scenes. The experimental results with different convolution operations are compared with the simulation results, exhibiting great agreement. Photo credits: https://rslab.ut.ac.ir/data.

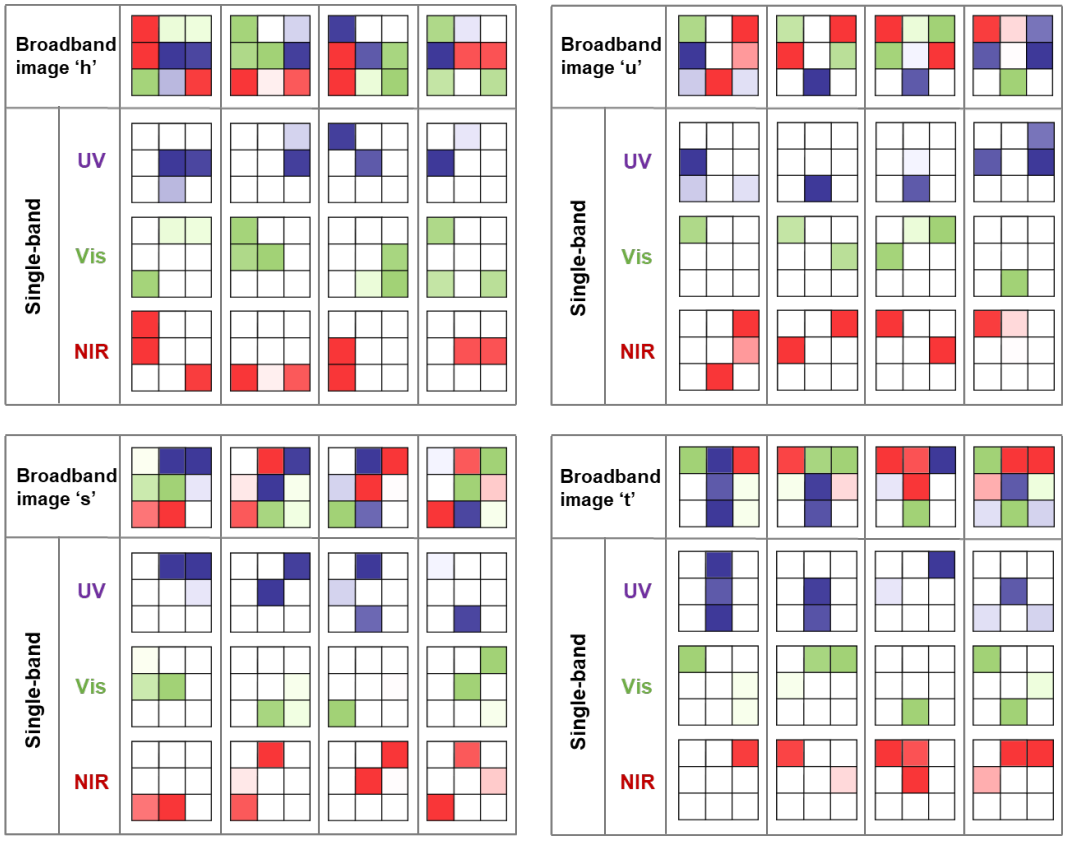

Supplementary Fig. 12. Partially broadband and corresponding single band-based image dataset for classifier training. The training broadband image database is composed of four different types of letters ('h', 'u', 's' and 't') with 3×3 pixels (9 binary digits). The total dataset includes 40 broadband images and 120 corresponding single-band images. Red, green and purple represent NIR (980 nm), Vis (532 nm) and UV (365 nm) light, respectively. The background noise with $\sigma = 0.2$ is represented with different coloured blocks.

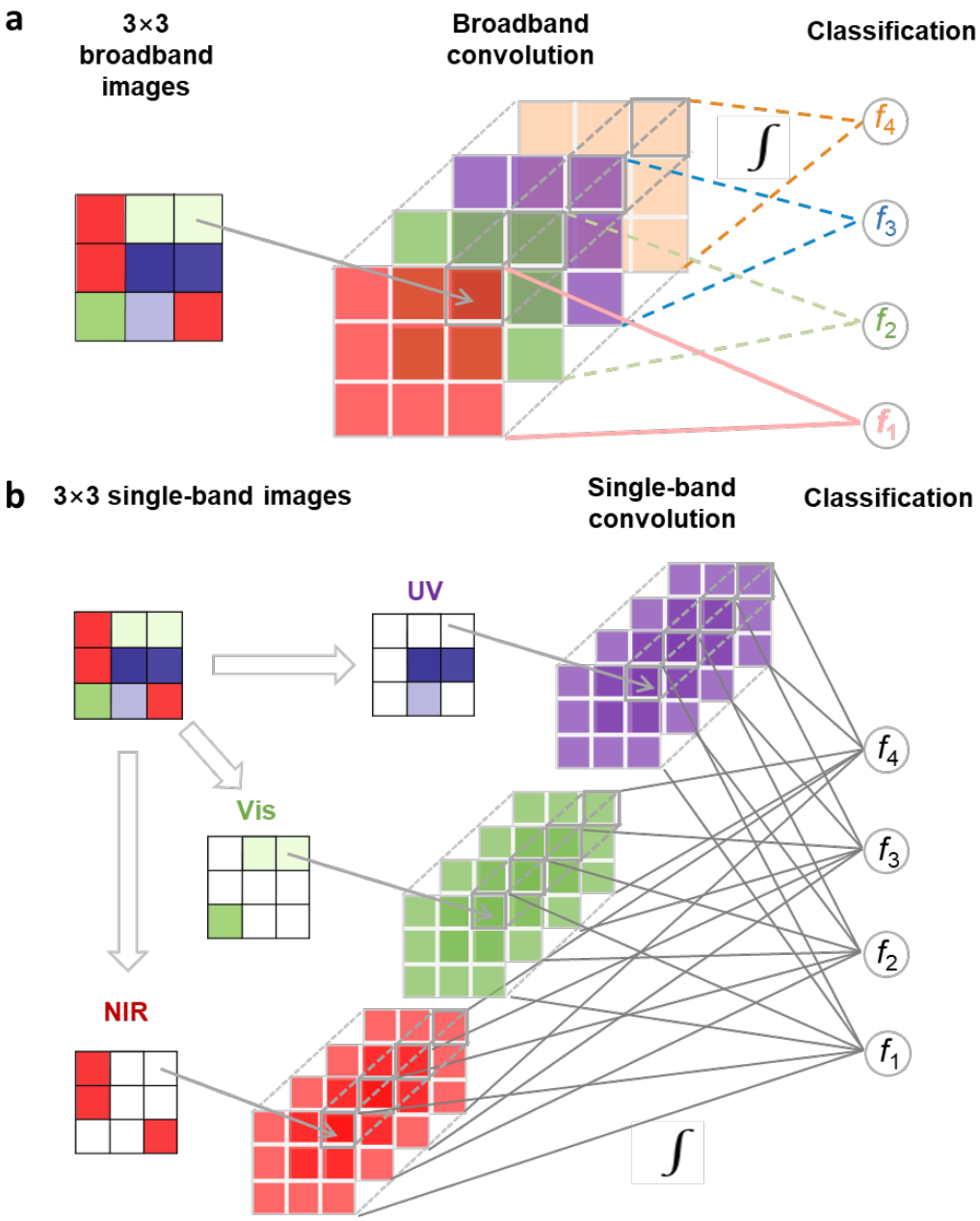

Supplementary Fig. 13. Schematic diagram of the training process for broadband and single-band image sensors. a, Schematic diagram of the training process for broadband photosensors used to recognize and classify broadband images, where different convolution kernels are represented by different colour mappings. We take the dot product of the grey value of the image and the weights (V_g) of each pixel, summing them to obtain the total current and identify the target letter for the input signal by comparing the standard parameters

[3,4]. The size, number, and pace of the broadband convolution kernel can be modulated in advance (as shown in the Methods). **b,** Schematic diagram of the training process for single-band convolution operations used to recognize and classify broadband images**.** Single-band convolution operations can only process optical signals within a specific wavelength, so it is necessary to split the broadband images and then identify and classify them separately. As a comparison, the in-sensor BCP can allow for end-to-end training by directly inputting the original broadband images.

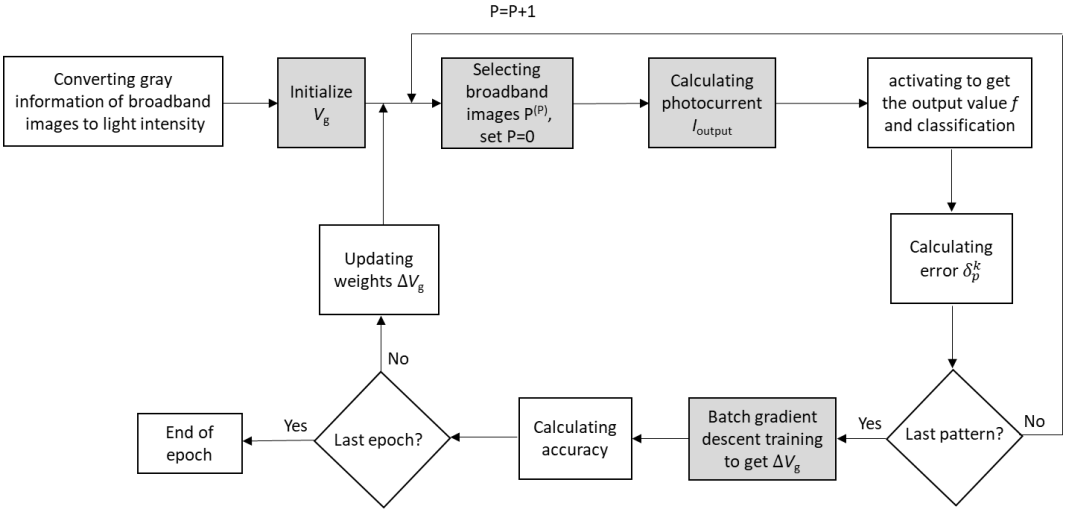

Supplementary Fig. 14. Flow chart of the training algorithm. The grey shaded boxes interact with the in-sensor BCP, and the white processing boxes are simulated using software.

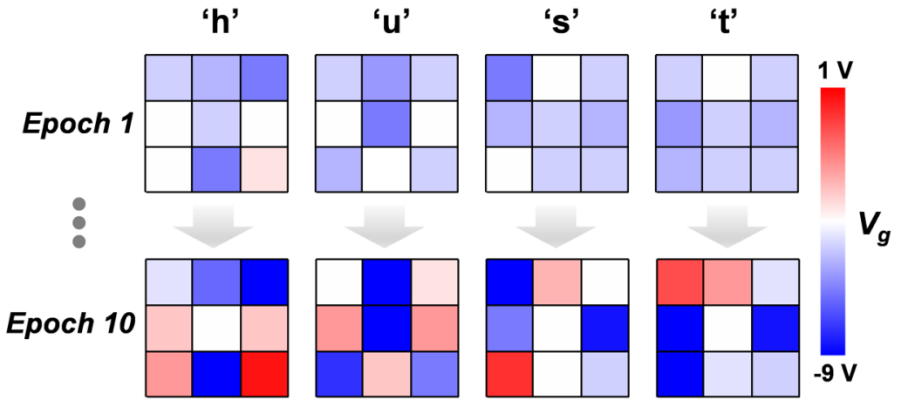

Supplementary Fig. 15. The weights distribution of the kernels varies with the number of training epoch. The heatmap for each pixel in the output image represents the corresponding weights in the 3×3 array, and the training time is 10 epochs.

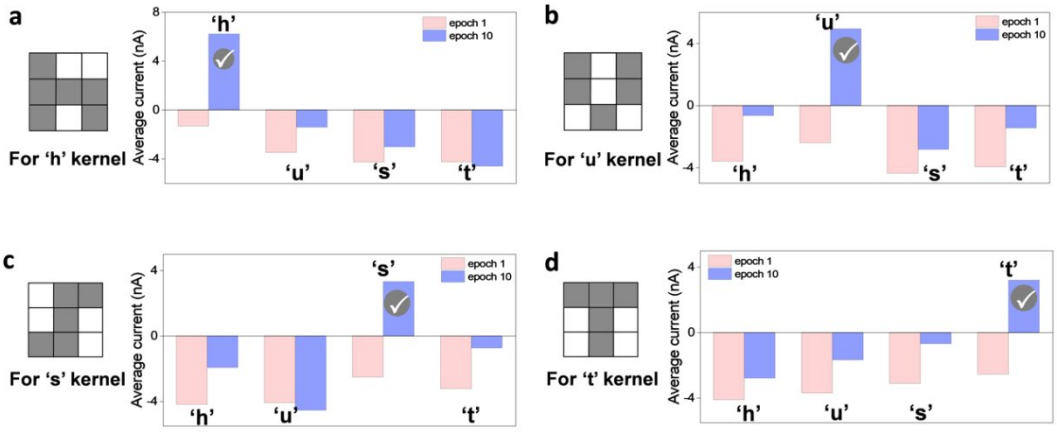

Supplementary Fig. 16. Comparison of the total output photocurrent under training epoch 1 and epoch 10. The total output value for the different convolution kernels f_1 (**a**) f_2 (**b**) f_3 (**c**) f_4 (**d**) in the process of in-situ training to recognize the broadband images ('h', 'u', 's' and 't'), where the images are accurately predicted when the correct convolution kernels has the largest activation.

In detail, the adaptive learning process have been demonstrated to identify image 'h' for the broadband convolution kernels, with the in-situ training 'h' (f_1) in different epochs. We can see that the corresponding total photocurrent for image 'h' is continuously increased from '-1.3 nA' in the initial state to '6.2 nA' in 10 epochs, which means that the recognition and classification capabilities of the convolution kernel (f_1) for image 'h' are continuously improved during the training process. In contrast, the recognition of images 'u', 's' and 't' by f_1 shows a completely opposite trend, where all output photocurrents show a negative distribution trend as the kernel weights are updated, indicating that these images doesn't meet the classification results (**a**). Similarly, broadband convolution kernels (f_2), (f_3), and (f_4) also specifically identify and classify images 'u', 's', and 't', respectively (**b**, **c**, and **d**).

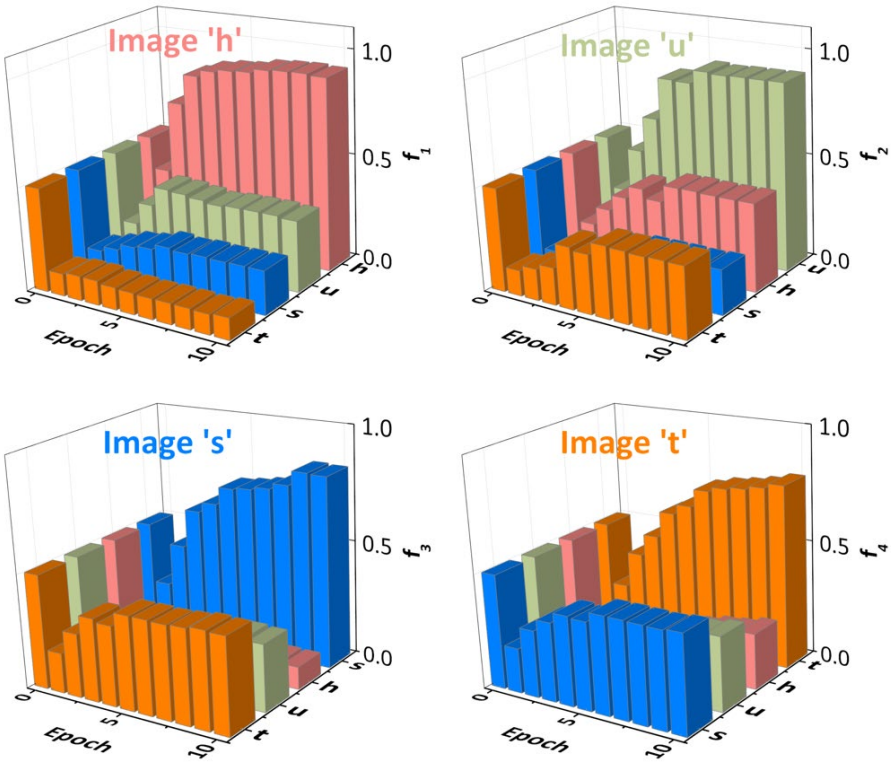

Supplementary Fig. 17. The average output photocurrent for different input letters varies with number of training epoch. Each histograms with the maximum output value (f_1, f_2, f_3 and f_4, respectively) represent the recognition results of the target letters.

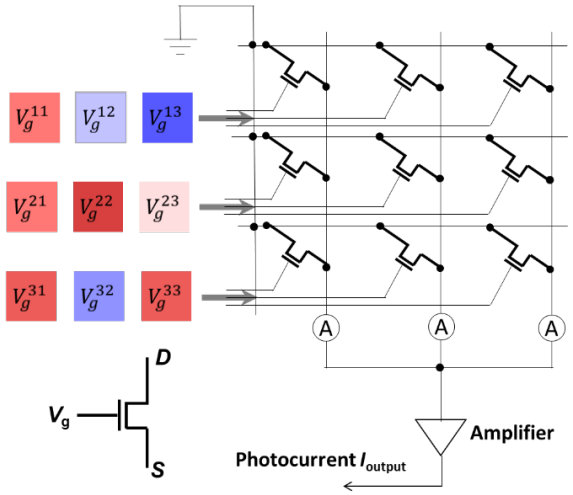

Supplementary Fig. 18. The circuit scheme based on 2D heterostructure devices array for implementing convolution processing, where electrical symbol represents the optoelectronic devices, and its photoresponse can be tuned independently by gate voltage. The output photocurrent represents the summation of photocurrent generated at individual devices in the array.

Supplementary Table 1: The total output photocurrent obtained for different images during the training process of convolution kernel 'h'. The table compares the total output photocurrent for the broadband convolution kernel (f_1) from epoch 1 to epoch 10 in the process of in-situ training for the letters ('h', 'u', 's' and 't'). As the number of training epoch increases, the weights distribution of kernels is continuously updated, and the output photocurrent presents a positive and negative bipolar distribution. The extracted total output photocurrent under training epochs 1 and 10 (marked red) is demonstrated in Supplementary Fig. 16a.

Kernel 'h'		Epoch0	Epoch1	Epoch2	Epoch3	Epoch4	Epoch5	Epoch6	Epoch7	Epoch8	Epoch9	Epoch10
I_{output} (nA)	h	0	-1.3319	1.908798	4.165521	4.604221	5.275238	5.415233	5.883787	6.340235	6.013309	6.207322
	u	0	-3.49792	-2.05751	-1.15702	-1.28002	-1.36373	-1.49575	-1.44263	-1.42191	-1.40092	-1.42692
	s	0	-4.27732	-3.72563	-3.36034	-3.13425	-3.001	-3.01952	-3.05364	-3.13561	-3.06741	-3.03413
	t	0	-4.26619	-4.19095	-4.35693	-4.50491	-4.72971	-4.68153	-4.70415	-4.77519	-4.7583	-4.62391

References

1 Wu, E. *et al.* Dynamically controllable polarity modulation of $MoTe_2$ field-effect transistors through ultraviolet light and electrostatic activation. *Sci. Adv.* **5**, eaav3430 (2019).

2 Oyedele, A. D. *et al.* $PdSe_2$: Pentagonal two-dimensional layers with high air stability for electronics. *J. Am. Chem. Soc.* **139**, 14090-14097 (2017).

3 Mennel, L. *et al.* Ultrafast machine vision with 2D material neural network image sensors. *Nature* **579**, 62-66 (2020).

4 Wang, C.-Y. *et al.* Gate-tunable van der Waals heterostructure for reconfigurable neural network vision sensor. *Sci. Adv.* **6**, eaba6173 (2020).